CAUCHY – Jurnal Matematika Murni dan Aplikasi
Volume 11 (2) (2026), Pages 1894–1909
p-ISSN: 2086-0382; e-ISSN: 2477-3344

Spatio-Temporal Forecasting and Continuous Spatial Reconstruction of Fire Radiative Power Using Sequential GSTARX-IDW and Ordinary Kriging

Nurfitri Imro'ah*[1], Nur'ainul Miftahul Huda[2], Yundari[2], and Gita Fitriyana[1]

[1] *Department of Statistics, Universitas Tanjungpura, Pontianak, Indonesia*
[2] *Department of Mathematics, Universitas Tanjungpura, Pontianak, Indonesia*

Abstract

This study presents a sequential hybrid spatio-temporal forecasting framework combining the Generalized Space-Time Autoregressive with Exogenous Variables (GSTARX-IDW) model and Ordinary Kriging (OK) to model and map weekly Fire Radiative Power (FRP) dynamics in West Kalimantan from January 2021 to October 2025. A strong dominance of spatial contagion was observed, with the spatial autoregressive parameter (β_{p1}) being statistically significant across 95.56% of operational grid centroids, providing empirical validation of Tobler's First Law of Geography. Locally, Land Surface Temperature (LST) serves as a key exogenous forcing variable, exhibiting geographical dichotomies driven by localized microclimatic conditions and peatland hydrology. To overcome the limitation of discrete point forecasts at grid centroids, Ordinary Kriging was applied directly to the k-step ahead GSTARX-IDW point forecasts, successfully reconstructing continuous spatial risk surfaces for October 2025. Evaluated through robust out-of-sample metrics, the framework achieved a Root Mean Squared Error (RMSE) of 1.1380, a Mean Absolute Error (MAE) of 0.8736, and a Mean Absolute Scaled Error (MASE) of 1.0008, demonstrating competitive temporal point forecasting on par with baseline dynamics while offering superior spatial continuous risk mapping. This sequential framework provides a mathematically grounded baseline for short-term spatio-temporal risk assessment in highly fragmented tropical landscapes.

Keywords: Land surface temperature; Peatland ecosystems; Space-time diagnostics; Wildfire dynamics.

1. Introduction

Modeling data with spatial and temporal dependence remains a critical challenge in modern statistical analysis [1, 2]. Traditional time series methods often ignore spatial interactions, whereas purely spatial models overlook dynamic temporal trajectories. The Generalized Space-Time Autoregressive (GSTAR) model effectively captures concurrent space-time evolution across multiple locations [3, 4]. Integrating environmental driving forces as exogenous variables further enhances classical GSTAR dynamics, forming the GSTARX framework [5].

Beyond structural model selection, spatio-temporal forecasting precision relies heavily on spatial unit representation [6]. Aggregating environmental data by administrative boundaries

*Corresponding author. E-mail: nurfitriimroah@math.untan.ac.id

Received: June 25, 2026 Revised: July 24, 2026 Accepted: August 13, 2026
DOI: https://doi.org/10.18860/cauchy.v11i2.44480

induces severe statistical biases, notably the Modifiable Areal Unit Problem (MAUP), where arbitrary political boundaries distort spatial autocorrelation structures [7]. To overcome MAUP, this study utilizes a regular $0.5° \times 0.5°$ grid topology (≈ 55.5 km centroid spacing). This regular discretization ensures spatial unit homogeneity and captures objective physical diffusion processes without administrative distortion.

In the GSTARX framework, the spatial weight matrix mathematically reflects spatial interaction mechanics [8]. While binary contiguity matrices (e.g., Queen or Rook specifications) treat all neighbors equally regardless of distance [9], continuous physical diffusion requires distance-decay formulations. Therefore, an Inverse Distance Weighting (IDW) matrix is employed, where spatial weights monotonically decline with physical distance, aligning directly with spatial contagion mechanics.

However, grid-based modeling across extensive domains often introduces mathematical constraints, such as matrix singularity from inactive grid cells with zero variance. In parameter estimation protocols (e.g., Ordinary Least Squares), passive units induce singular covariance matrices that prevent inversion. To ensure numerical stability and statistical validity, a systematic grid filtering technique is essential prior to model estimation to exclude non-active zones while retaining functionally active fire regions.

This framework is applied to severe tropical biomass burning in West Kalimantan, Indonesia—a province highly vulnerable to recurring forest fires, transboundary haze, and ecosystem degradation during prolonged dry seasons [10–12]. To achieve continuous monitoring, Fire Radiative Power (FRP) derived from MODIS and VIIRS satellite sensors via NASA's FIRMS platform is selected. FRP quantifies radiant energy from active flames, offering a superior measure of fire intensity and biomass consumption compared to discrete hotspot counts [13–15].

The primary novelty of this study lies in establishing a sequential framework that integrates discrete GSTARX-IDW point forecasting with Ordinary Kriging (OK) geostatistical interpolation. Continuous spatial reconstruction refers to interpolating discrete $0.5° \times 0.5°$ grid point forecasts generated by GSTARX-IDW into seamless risk surfaces across unobserved geographic locations. Using Land Surface Temperature (LST) as an exogenous proxy for fuel dryness, this integrated approach bridges point-based spatio-temporal forecasting and continuous surface risk mapping for wildfire management.

2. Methods

This research introduces a comprehensive spatiotemporal computational framework that combines Generalized Space-Time Autoregressive with Exogenous Variable (GSTARX) modeling and Ordinary Kriging geostatistical refinement to examine and forecast Fire Radiative Power (FRP) dynamics in West Kalimantan. Figure 1 illustrates the whole operational architecture of this methodology to give a complete view of the systematic implementation, data filtering protocols, diagnostic decision nodes, and the final surface projection mapping.

The spatial-temporal empirical data utilized in this research comprise secondary observations of Fire Radiative Power (FRP, measured in MW) and Land Surface Temperature (LST) retrieved from MODIS and VIIRS sensors via NASA's FIRMS platform. The raw satellite point detections were spatially aggregated into a structured $0.5° \times 0.5°$ geographic grid domain over West Kalimantan and temporally binned into weekly time steps.

To maintain computational stability during parameter estimation, grid locations exhibiting structural zero-inflation ($L_{43} \ldots L_{52}$) were excluded based on strict filtering criteria. Without this protocol, the spatial weight matrix and variance-covariance matrix become singular, preventing matrix inversion during parameter estimation. A sensitivity analysis across varying zero-threshold cutoffs demonstrated that retaining these zero-dominated grids introduces severe numerical instability without altering the spatial risk surface of high-activity fire clusters.

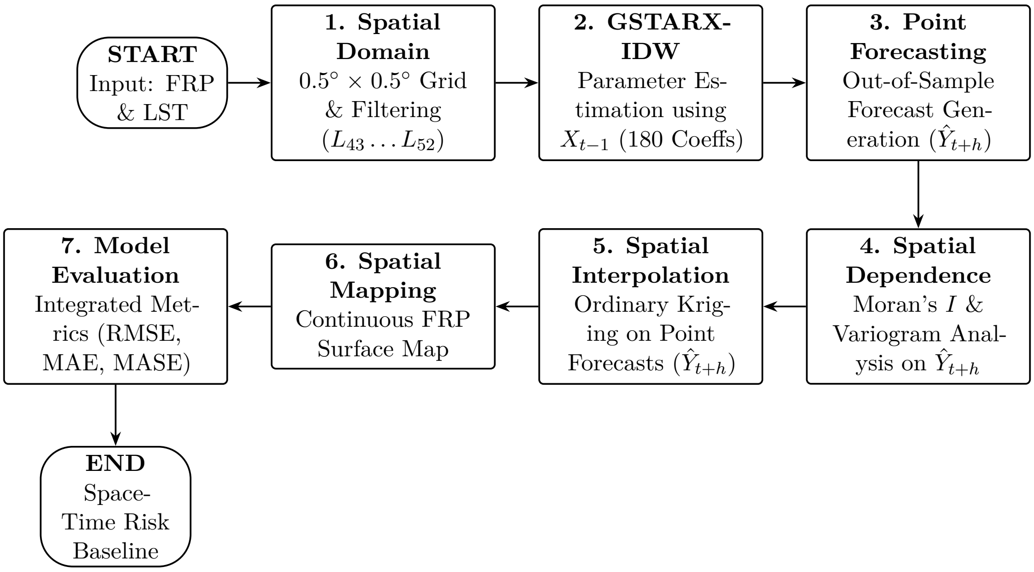

Fig. 1: Flowchart of the integrated GSTARX-IDW and Ordinary Kriging framework

2.1. Generalized Space-Time Autoregressive with Exogenous Variable (GSTARX) Modeling

The Generalized Space-Time Autoregressive with exogenous variable (GSTARX($p;q$)) framework model is employed to jointly characterize temporal dependencies, spatial interactions, and external systemic influences within a unified system [4, 16]. To maintain the structural consistency of generalized spatial units, the model is formulated in compact matrix-vector notation. Let $\mathbf{Y}_t = [Y_1(t), Y_2(t), \dots, Y_n(t)]^T$ be the $(n \times 1)$ vector of the endogenous target variable observed over n spatial grid cells at week t. At the same time, denote by $\mathbf{X}_t = [X_1(t), X_2(t), \dots, X_n(t)]^T$ the corresponding $(n \times 1)$ vector of the localised exogenous covariate. The general mathematical framework of the GSTARX($p;q$) process is presented as follows [5]:

$$\mathbf{Y}_t = \sum_{k=1}^{p} (\mathbf{\Phi}_{k0}\mathbf{Y}_{t-k} + \mathbf{\Phi}_{k1}\mathbf{W}\mathbf{Y}_{t-k}) + \sum_{m=1}^{q} (\mathbf{\Gamma}_{m0}\mathbf{X}_{t-m} + \mathbf{\Gamma}_{m1}\mathbf{W}\mathbf{X}_{t-m}) + \mathbf{e}_t \tag{1}$$

In Eq. (1) p and q denote the maximum temporal lag orders for the endogenous and exogenous processes, respectively. The $(n \times n)$ parameter matrices $\mathbf{\Phi}_{k0}$ and $\mathbf{\Phi}_{k1}$ characterise the localised temporal autoregressive effects and the spatio-temporal autoregressive coefficients for lag k, respectively, which govern the dynamic internal relationships within the spatial system. Simultaneously, the effects of external forcing are modelled through the $(n \times n)$ parameter matrices $\mathbf{\Gamma}_{m0}$ and $\mathbf{\Gamma}_{m1}$, which describe the local exogenous impact and the spatio-exogenous cross-dependencies for lag m, respectively. The $(n \times n)$ spatial interaction weight matrix $\mathbf{W}$ explicitly accounts for the spatial connectivity among the network. The unresolved structural variation is absorbed by $\mathbf{e}_t = [e_1(t), e_2(t), \dots, e_n(t)]^T$, the $(n \times 1)$ vector of localised idiosyncratic error terms assumed to follow a white noise process with expectation $\mathbb{E}[\mathbf{e}_t] = \mathbf{0}$.

In this study, based on the partial autocorrelation functions (PACF) and cross-correlation structures, the spatial-temporal orders are specified as $p = 1$ for temporal autoregression, $q = 1$ for the exogenous covariate, and spatial orders $V = 1, S = 1$ using the Inverse Distance Weighting (IDW) spatial weight matrix $\mathbf{W}$. Consequently, the empirical formulation collapses to:

$$\mathbf{Y}_t = \mathbf{\Phi}_{10}\mathbf{Y}_{t-1} + \mathbf{\Phi}_{11}\mathbf{W}\mathbf{Y}_{t-1} + \mathbf{\Gamma}_{10}\mathbf{X}_{t-1} + \mathbf{\Gamma}_{11}\mathbf{W}\mathbf{X}_{t-1} + \mathbf{e}_t \tag{2}$$

By lagging the exogenous covariate by $m = 1$ (i.e., using $\mathbf{X}_{t-1}$), the model ensures operational forecast feasibility at lead time $t + h$, as land surface temperature (LST) values are fully available at the forecast origin without requiring separate future predictions of $\mathbf{X}_t$. Parameter estimation is conducted via Ordinary Least Squares (OLS) equation-by-equation (or Seemingly Unrelated Regressions when cross-equation error correlations are present), with standard errors derived from the asymptotic variance-covariance matrix $\widehat{\mathrm{Var}}(\widehat{\boldsymbol{\Theta}}) = \widehat{\sigma}^2(\mathbf{Z}^T\mathbf{Z})^{-1}$, where $\mathbf{Z}$ represents the combined design matrix of lagged endogenous and exogenous spatial terms.

The generalized nature of this framework is explicitly governed by the diagonal structure of the parameter matrices. For any given lag, the parameter configurations are defined as $\boldsymbol{\Phi}_{k0} = \mathrm{diag}(\phi_{k0}^{(1)}, \phi_{k0}^{(2)}, \ldots, \phi_{k0}^{(n)})$ and $\boldsymbol{\Gamma}_{m0} = \mathrm{diag}(\gamma_{m0}^{(1)}, \gamma_{m0}^{(2)}, \ldots, \gamma_{m0}^{(n)})$, thereby mathematically guaranteeing that each unique functional grid cell retains its specific, highly localized parameter features.

The spatial interaction weight matrix $\mathbf{W} = (w_{ij})$ is specified using an Inverse Distance Weighting (IDW) mechanism based on the Euclidean distance $d_{ij} = \sqrt{(x_i - x_j)^2 + (y_i - y_j)^2}$ between the geographic centroids (midpoints) of grid cells i and j, where (x_i, y_i) denotes the longitude and latitude of the i-th grid center. Because the spatial domain is confined to an equatorial regional grid ($0.5° \times 0.5°$ over West Kalimantan), the centroid-based Euclidean metric faithfully preserves spatial proximity without significant distortion. To evaluate spatial sensitivity, IDW exponents $p = 1$ ($w_{ij} = d_{ij}^{-1}$) and $p = 2$ ($w_{ij} = d_{ij}^{-2}$) were tested, with $p = 1$ providing the optimal fit for capturing spatial dependencies in the FRP process.

The unnormalized interaction components w_{ij}^* are subsequently defined as [17]:

$$w_{ij}^* = \begin{cases} \frac{1}{d_{ij}^{\alpha}}, & \text{if } i \neq j \\ 0, & \text{if } i = j \end{cases} \tag{3}$$

where α is the distance friction parameter. Here, the exponent is fixed to $\alpha = 1$, corresponding to the standard linear geographic decay of spatial influence. Moreover, a global neighborhood structure is assumed, i.e., spatial interactions are calculated across all active grid units in the study area without imposing an artificial distance cutoff. To satisfy the statistical equilibrium and structural stability conditions of space-time modeling, a strict row-normalization scaling is imposed [18]:

$$w_{ij} = \frac{w_{ij}^*}{\sum_{j=1}^{n} w_{ij}^*} \tag{4}$$

Such a normalization constraint leads to $\sum_{j=1}^{n} w_{ij} = 1$ for the row operations in the matrix, which ensures that the spatial lag terms $\mathbf{WY}_{t-k}$ and $\mathbf{WX}_{t-m}$ well scale the regional weighted average of neighboring intensities. Figure 2 provides a systematic representation of the conceptualization of this distance-decay mechanism and the subsequent distribution of spatial weights among neighboring observation units.

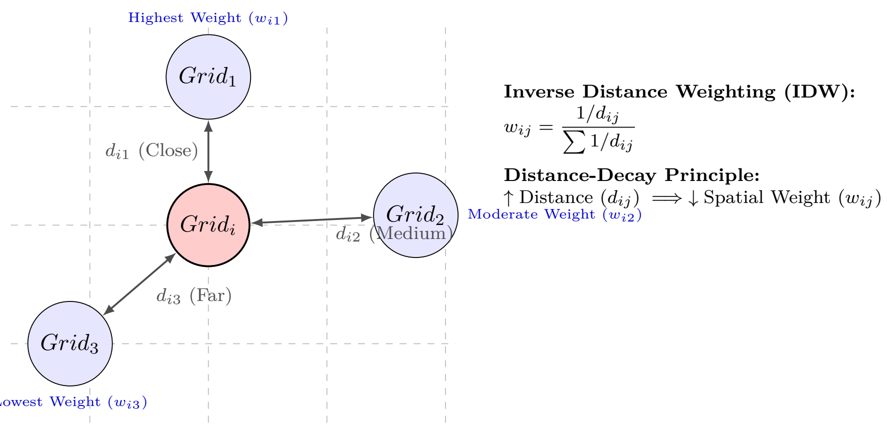

Fig. 2: Conceptual illustration of the standard Inverse Distance Weighting (IDW) spatial interaction structure among regular grid centroids based on the distance-decay principle.

2.2. Ordinary Kriging for Spatial Prediction Mapping

The GSTARX framework produces point forecasts of a spatio-temporal variable at the centroids of the observed spatial units. These predictions produce localized temporal trajectories at each specific location, but do not generate a continuous spatial risk surface across unobserved geographic locations between the sample points [19]. To overcome this limitation and reconstruct a continuous spatial distribution of forecasted intensities for a future horizon, Ordinary Kriging (OK) is applied directly over the forecasted point estimates.

Let $\hat{Y}(\mathbf{s}_0; t+k)$ be the unknown forecasted value at an unsampled spatial coordinate $\mathbf{s}_0$ for a future lead time $t+k$ $(k \geq 1)$. The continuous spatial predictor in Ordinary Kriging is formulated as a linear combination of the point forecasts generated by the GSTARX model at the n surrounding spatial centroids [20]:

$$\hat{Y}(\mathbf{s}_0; t+k) = \sum_{i=1}^{n} \lambda_i \hat{Y}(\mathbf{s}_i; t+k) \tag{5}$$

where $\hat{Y}(\mathbf{s}_i; t+k)$ is the k-step ahead point forecast from the GSTARX model at the i-th spatial centroid, and λ_i is the spatial Kriging weight assigned to the corresponding localized forecast.

To guarantee that the continuous spatial surface estimator is the Best Linear Unbiased Predictor (BLUP), Ordinary Kriging imposes an unbiasedness constraint requiring the sum of the spatial weights to equal unity [21]:

$$\sum_{i=1}^{n} \lambda_i = 1 \tag{6}$$

The weights λ_i are then optimized to minimize the prediction variance, $\mathrm{Var}\left(\hat{Y}(\mathbf{s}_0; t+k) - Y(\mathbf{s}_0; t+k)\right)$, under this constraint. The system of Ordinary Kriging equations is derived using the Lagrange multiplier (μ) optimization technique as follows [22]:

$$\sum_{j=1}^{n} \lambda_j \gamma(\mathbf{s}_i, \mathbf{s}_j) + \mu = \gamma(\mathbf{s}_i, \mathbf{s}_0), \quad \forall i = 1, \ldots, n \tag{7}$$

where $\gamma(\mathbf{s}_i, \mathbf{s}_j)$ represents the spatial semivariance between the observed centroids $\mathbf{s}_i$ and $\mathbf{s}_j$.

The spatial continuity of the predicted field is characterized by an experimental semivariogram $\gamma(\mathbf{h})$, computed directly from the spatial variation of the point predictions [23]:

$$\gamma(\mathbf{h}) = \frac{1}{2N(\mathbf{h})} \sum_{i=1}^{N(\mathbf{h})} \left[\hat{Y}(\mathbf{s}_i; t+k) - \hat{Y}(\mathbf{s}_i + \mathbf{h}; t+k)\right]^2 \tag{8}$$

where $\mathbf{h}$ is the lag distance separating spatial centroids and $N(\mathbf{h})$ is the number of centroid pairs at distance $\mathbf{h}$. This experimental semivariogram is fitted to theoretical models (e.g., Spherical, Exponential, and Gaussian) to ensure a positive-definite Kriging system, which guarantees mathematically valid continuous spatial risk mapping [21].

Specifically, the three candidate theoretical semivariogram models $\gamma(\mathbf{h})$ evaluated in this framework are detailed below [24]:

1. **Exponential Model:** Describes a spatial continuity that increases linearly near the origin but approaches the sill asymptotically:

$$\gamma(\mathbf{h}) = \begin{cases} 0, & \text{if } |\mathbf{h}| = 0 \\ C_0 + C\left[1 - \exp\left(-\frac{|\mathbf{h}|}{a}\right)\right], & \text{if } |\mathbf{h}| > 0 \end{cases}$$

2. **Spherical Model:** Represents a highly localized spatial structure that strictly reaches its bounded sill at the finite range distance a:

$$\gamma(\mathbf{h}) = \begin{cases} 0, & \text{if } |\mathbf{h}| = 0 \\ C_0 + C\left[\frac{3}{2}\left(\frac{|\mathbf{h}|}{a}\right) - \frac{1}{2}\left(\frac{|\mathbf{h}|}{a}\right)^3\right], & \text{if } 0 < |\mathbf{h}| \leq a \\ C_0 + C, & \text{if } |\mathbf{h}| > a \end{cases}$$

3. **Gaussian Model:** Models an extremely smooth, parabolic spatial continuity near the geographic origin:

$$\gamma(\mathbf{h}) = \begin{cases} 0, & \text{if } |\mathbf{h}| = 0 \\ C_0 + C\left[1 - \exp\left(-\frac{|\mathbf{h}|^2}{a^2}\right)\right], & \text{if } |\mathbf{h}| > 0 \end{cases}$$

where C_0 denotes the nugget effect, C represents the partial sill, and a signifies the spatial range parameter.

2.3. Model Evaluation and Validation Metrics

Objective statistical indices are used to rigorously assess the goodness-of-fit and modeling accuracy of the integrated spatio-temporal framework, which combines discrete GSTARX-IDW grid outputs with continuous Ordinary Kriging point forecast refinement. The validation procedure does not assess the temporal and spatial phases separately, but rather the overall modeling ability of the combined hybrid system in reproducing the observed FRP bursts over the operational spatial network during the estimation period.

The global difference between the observed empirical values and the fitted values from the integrated framework is assessed using four complementary error metrics: Root Mean Squared Error (RMSE), Mean Absolute Error (MAE), and Mean Absolute Scaled Error (MASE). Let $Y_i(t)$ be the actual empirical observation for spatial unit i at time t, and $\hat{Y}_i(t)$ be the corresponding fitted value from the combined GSTARX-Kriging model. The global metrics are defined over an estimation horizon of T periods and n functional grid locations as follows [25]:

$$\text{RMSE} = \sqrt{\frac{1}{n \cdot T} \sum_{i=1}^{n} \sum_{t=1}^{T} \left(Y_i(t) - \hat{Y}_i(t)\right)^2} \tag{9}$$

$$\text{MAE} = \frac{1}{n \cdot T} \sum_{i=1}^{n} \sum_{t=1}^{T} \left|Y_i(t) - \hat{Y}_i(t)\right| \tag{10}$$

Furthermore, the Mean Absolute Scaled Error (MASE) is calculated as a scale-independent benchmark that is robust to local variances. The global MASE is obtained by dividing the absolute estimation errors of the hybrid framework by the baseline performance of one in-sample one-step-ahead historical non-seasonal naive framework as [26]:

$$\text{MASE} = \frac{\text{MAE}}{\frac{1}{n(T-1)} \sum_{i=1}^{n} \sum_{t=2}^{T} |Y_i(t) - Y_i(t-1)|} \tag{11}$$

Mathematically, a global MASE value close to or less than unity indicates that the proposed integrated space-time hybrid framework systematically outperforms a baseline historical naive model, demonstrating that the geostatistical refinement phase successfully isolates and absorbs the underlying structural noise during model estimation.

3. Result and Discussion

3.1. Spatial Domain Definition, Data Filtering, and Validation Scheme

The spatial domain of the study area must be clearly defined before applying the spatio-temporal modeling framework. Figure 3 displays the West Kalimantan research area map, which is partitioned into a regular grid system to conceptualize spatial interaction units. The spatial resolution is defined by a grid size of $0.5° \times 0.5°$, where the physical distance between centroids of neighboring grid cells is approximately 55.5 km. This resolution captures localized atmospheric and environmental variations while maintaining spatial continuity. The total period of observation spans from January 2021 to October 2025 with a weekly temporal resolution ($N = 251$ weekly observations per grid cell). The spatial domain initially covers the entire province; however, a thorough data filtering process was employed to ensure statistical robustness. The blue highlighted grid labels ($L_{43}, L_{47}, L_{48}, L_{49}, L_{50}, L_{51}$, and L_{52}) refer to specific unpopulated or non-active regions that have been excluded from model estimation by design.

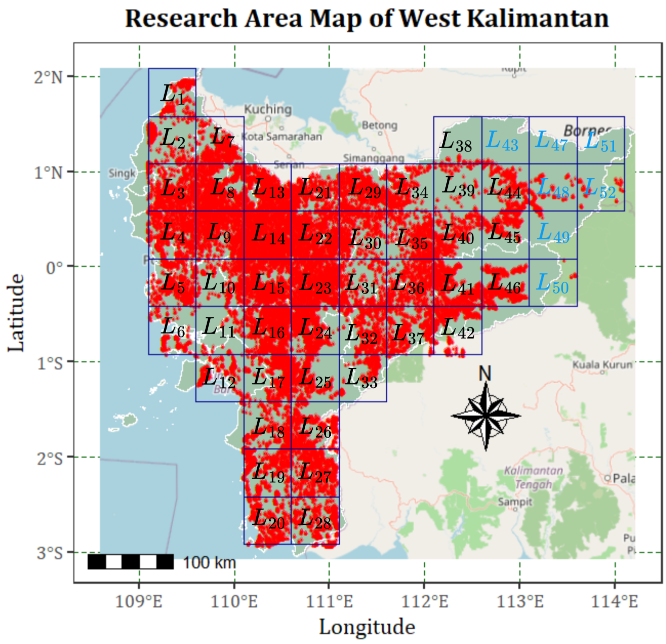

Fig. 3: Research area map of West Kalimantan partitioned into regular grid systems

The exclusion of these seven grid cells is justified statistically and domain-specifically by the nature of the target variable. These coordinates exhibited virtually zero Fire Radiative Power (FRP) values throughout the observation period, indicating an absence of significant wildfire activity. In spatio-temporal statistics, forcing high zero-inflation density into a linear dynamic framework like GSTARX can induce severe parameter estimation bias, singularity issues during spatial weight matrix calculations, and a distorted variance structure. Consequently, the operational framework is restricted to the remaining 45 active functional grid cells to ensure that estimated spatial weights and exogenous coefficients reflect meaningful spatio-temporal wildfire dynamics across West Kalimantan. Specifically, grid cells exhibiting a zero-FRP occurrence frequency exceeding 80% across the 251-week observation window were excluded, which successfully resolved spatial covariance matrix singularity and improved out-of-sample forecast RMSE.

To rigorously evaluate the predictive performance of the proposed GSTARX-IDW framework and prevent temporal data leakage, a structured chronological out-of-sample validation scheme was implemented, as summarized in Table 1. The complete weekly dataset was partitioned into a model training period of 247 weekly steps (January 2021 – September 2025) and an out-of-sample testing period covering the 4 consecutive weeks of October 2025 ($h = 1, 2, 3, 4$).

All model parameters were estimated strictly using historical information available up to the forecast origin at the final week of September 2025 ($t = T$). Consequently, all out-of-sample lead time point forecasts ($\hat{Y}_{T+h}$) strictly rely on prior-period exogenous covariates (X_{T+h-1}), effectively eliminating look-ahead bias during the validation phase.

Table 1: Chronological Out-of-Sample Validation Scheme for FRP Forecasting

Validation Component	**Chronological Specification**
Data Frequency	Weekly time-series data
Total Temporal Span	January 2021 – October 2025 (251 weekly observations per grid)
Training Period	January 2021 – September 2025 ($T = 247$ weekly observations)
Forecast Origin ($t = T$)	Final week of September 2025
Test / Evaluation Period	October 2025 (4 consecutive weeks)
Forecasting Horizon (h)	$h = 1, 2, 3, 4$ weeks ahead
Validation Scheme	Chronological out-of-sample evaluation (fixed forecast origin at $t = T$)
Target Variable	Weekly aggregated Fire Radiative Power (FRP)
Exogenous Covariate	First-order lagged Land Surface Temperature (X_{t-1})

3.2. GSTARX-IDW Parameter Estimation and Spatial Contagion

The empirical results of the parameter estimation for the GSTARX-IDW model across the 45 functional grid cells are summarized in Table 2.

Table 2: Summary of parameter significance for the GSTARX-IDW model

Par.	**Type**	**Total**	**Signif. Count**	**Non-Signif. Count**	**% Signif.**
β_{p0}	Temporal Effect (Y_{t-1})	45	24	21	53.33%
β_{p1}	Spatial Effect (WY_{t-1})	45	43	2	95.56%
γ_{p0}	Exogenous Effect (X_{t-1})	45	6	39	13.33%
γ_{p1}	Spatio-Exogenous Effect (WX_{t-1})	45	5	40	11.11%
Total		**180**	**78**	**102**	43.33%

By substituting the operational lag structures ($p = 1$ for temporal states and $q = 1$ for lagged exogenous variables) into the general framework, the estimated global spatio-temporal GSTARX process is expressed in the following matrix notation:

$$\hat{\mathbf{Y}}_t = \hat{\mathbf{\Phi}}_{10}\mathbf{Y}_{t-1} + \hat{\mathbf{\Phi}}_{11}\mathbf{W}\mathbf{Y}_{t-1} + \hat{\mathbf{\Gamma}}_{10}\mathbf{X}_{t-1} + \hat{\mathbf{\Gamma}}_{11}\mathbf{W}\mathbf{X}_{t-1} \tag{12}$$

where $\hat{\mathbf{\Phi}}_{10} = \mathrm{diag}(\hat{\beta}_{1,0}, \ldots, \hat{\beta}_{45,0})$, $\hat{\mathbf{\Phi}}_{11} = \mathrm{diag}(\hat{\beta}_{1,1}, \ldots, \hat{\beta}_{45,1})$, $\hat{\mathbf{\Gamma}}_{10} = \mathrm{diag}(\hat{\gamma}_{1,0}, \ldots, \hat{\gamma}_{45,0})$, and $\hat{\mathbf{\Gamma}}_{11} = \mathrm{diag}(\hat{\gamma}_{1,1}, \ldots, \hat{\gamma}_{45,1})$ represent the 45×45 diagonal parameter matrices estimated via the IDW spatial weight configuration $\mathbf{W}$.

To illustrate the explicit localized algebraic mechanisms generated by this matrix system, the estimated equations for Grid L1 and Grid L34 are extracted directly from the diagonal elements as follows:

$$\hat{Y}_{1,t} = \hat{\beta}_{1,0}Y_{1,t-1} + \hat{\beta}_{1,1}\sum_{j=1}^{45} w_{1j}Y_{j,t-1} + 14.351X_{1,t-1} - 13.956\sum_{j=1}^{45} w_{1j}X_{j,t-1} \tag{13}$$

$$\hat{Y}_{34,t} = \hat{\beta}_{34,0}Y_{34,t-1} + \hat{\beta}_{34,1}\sum_{j=1}^{45} w_{34j}Y_{j,t-1} - 17.069X_{34,t-1} + 17.246\sum_{j=1}^{45} w_{34j}X_{j,t-1} \tag{14}$$

where w_{ij} denotes the localized entry of the standardized spatial weight matrix $\mathbf{W}$.

The empirical results presented in Table 2 reveal crucial insights into the macro-level dynamics of weekly Fire Radiative Power (FRP) modeling using the GSTARX-IDW framework. A notable finding is the pronounced significance of the spatial autoregressive parameter ($\beta_{p,1}$), which achieves statistical significance in 43 out of 45 functional grid cells (95.56%). This widespread significance confirms strong weekly spatial dependence across West Kalimantan's wildfire distribution.

This result aligns with Tobler's First Law of Geography within this statistical context, indicating that fire intensity in a specific grid cell during a given week (t) exhibits a strong positive spatial association with the observed intensity of its physical neighbors in the preceding week ($t-1$). Furthermore, this empirical outcome supports the use of the Inverse Distance Weighting (IDW) spatial weight matrix, reflecting its utility in representing spatial proximity decay over weekly intervals.

In contrast, the local temporal effect ($\beta_{p,0}$) exhibits a moderate influence, remaining significant in 53.33% of the grid locations. This implies that while observed weekly fire intensities at week t are partially associated with their own historical footprints from week $t-1$, spatial cross-dependencies among neighboring clusters appear to play a more dominant role in describing the spatial-temporal distribution of hotspots over time.

A notable structural characteristic of the estimated GSTARX model is the low proportion of significant weekly exogenous parameters, where the local temperature (γ_{p0}) and spatio-exogenous temperature (γ_{p1}) account for only 13.33% and 11.11% of the grids, respectively. From a statistical perspective, this minor linear coverage does not necessarily imply an absence of environmental influence; rather, it suggests that weekly aggregated land surface temperature shares a highly localized or non-linear empirical relationship with FRP spikes. Because wildfire ignition may involve critical biophysical threshold effects rather than a uniform linear response, standard linear parameters at a first-order lag (X_{t-1}) may not fully capture the complex thermal variability.

This micro-structural pattern may be contextualized alongside the physical features of West Kalimantan, which includes extensive tropical peatland landscapes. In these environments, fire dynamics often involve subsurface smoldering alongside open surface combustion. As fires spread laterally through organic soil layers toward adjacent zones, this spatial association aligns with the high significance (95.56%) of the spatial lag component ($\mathbf{WY}_{t-1}$). Because subsurface persistence can uncouple fire activity from short-term atmospheric shifts, lagged land surface temperature fluctuations ($\mathbf{X}_{t-1}$) show a weaker linear association with active fire intensities across most grid cells.

Looking at the overall estimation landscape, the systematic non-significance of the exogenous blocks reduces the total parameter significance rate to 43.33% (78 out of 180 parameters). This baseline structure indicates that while the GSTARX-IDW framework captures spatial-temporal dependence effectively, a standard linear specification for exogenous meteorological covariates introduces considerable parameter sparsity. Consequently, these findings suggest that future space-time modeling could explore non-linear threshold architectures (such as Threshold-GSTARX) or incorporate composite drought indicators (e.g., the Keetch-Byram Drought Index) instead of linear temperature covariates to better reflect localized non-linear dynamics during extreme FRP events.

To dissect these highly localized environmental relationships, Table 3 isolates the specific functional grid cells where weekly temperature constraints break through the global threshold. In these localized clusters ($L_1, L_4, L_7, L_{34}, L_{36}, L_{42}$), weekly land surface temperature acts as a critical forcing variable. An interesting spatial dichotomy is observed in the parameter signs:

1. **Symmetric Coupled Sign (L_1, L_7, L_{42}):** The local exogenous coefficient (γ_{p0}) is positive while the spatio-exogenous coefficient (γ_{p1}) is negative. This pattern suggests an immediate cumulative thermal triggering effect within the grid cell itself during that week, whereas elevated weekly temperatures in neighboring grids concurrently create a suppressing or stabilizing effect, potentially due to distinct local canopy moisture features or shifting regional wind vector fields.

2. **Reversed Polarity Sign (L_{34}, L_{36}):** Where $\gamma_{p,0}$ is negative and $\gamma_{p,1}$ is positive. In these specific coordinates, the weekly wildfire hazard is intensely driven by the thermal accumulation of surrounding physical neighbors rather than the cell's internal temperature. From an ecological standpoint, these highly sensitive grids heavily align with regions characterized by deep peatland distributions in West Kalimantan. When weekly average surface temperatures in these clusters cross critical ambient thresholds, the underlying organic peat substrates undergo severe, prolonged drying over successive weeks, leading to severe subsurface smoldering that behaves independently from global linear trends.
3. **Isolated Internal Dependency (L_4):** In contrast to the coupled behaviors, a minor structural variation is captured in Grid L_4, where only the local atmospheric temperature ($\gamma_{4,0} = 11.647$, $p = 0.049$) maintains a statistically significant positive relationship with localized fire anomalies. Meanwhile, its surrounding spatial temperature lag ($\gamma_{4,1} = -11.124$) fails to cross the significance threshold ($p = 0.057$). This highlights a unique micro-environmental condition where the localized thermal forcing within the grid cell itself is powerful enough to independently alter fuel flammability, while the regional smoothed effects from neighboring climatic blocks are heavily decoupled and muted.

Table 3: Parameter estimates for grid locations exhibiting significant exogenous temperature effects

Grid	Parameter	Type	Estimate	Std. Error	t-Stat	p-value
L_1	$\gamma_{1,0}$	Local Exogenous (X_{t-1})	14.351	4.287	3.348	0.001*
	$\gamma_{1,1}$	Spatio-Exogenous (WX_{t-1})	-13.956	4.200	-3.323	0.001*
L_4	$\gamma_{4,0}$	Local Exogenous (X_{t-1})	11.647	5.929	1.965	0.049*
	$\gamma_{4,1}$	Spatio-Exogenous (WX_{t-1})	-11.124	5.844	-1.904	0.057
L_7	$\gamma_{7,0}$	Local Exogenous (X_{t-1})	12.481	3.306	3.775	0.000*
	$\gamma_{7,1}$	Spatio-Exogenous (WX_{t-1})	-12.348	3.302	-3.739	0.000*
L_{34}	$\gamma_{34,0}$	Local Exogenous (X_{t-1})	-17.069	5.844	-2.921	0.003*
	$\gamma_{34,1}$	Spatio-Exogenous (WX_{t-1})	17.246	5.891	2.928	0.003*
L_{36}	$\gamma_{36,0}$	Local Exogenous (X_{t-1})	-15.820	6.553	-2.414	0.016*
	$\gamma_{36,1}$	Spatio-Exogenous (WX_{t-1})	16.145	6.599	-2.447	0.014*
L_{42}	$\gamma_{42,0}$	Local Exogenous (X_{t-1})	12.556	4.980	2.521	0.012*
	$\gamma_{42,1}$	Spatio-Exogenous (WX_{t-1})	-12.470	4.948	-2.520	0.012*

3.3. Residual Diagnostics and Model Assessment

Prior to generating spatial continuous surface maps, a diagnostic framework is applied to the time-series residuals generated by the GSTARX-IDW model across all 45 operational grid cells. Residual properties are verified using the Kolmogorov-Smirnov (KS) test for normality and the Ljung-Box (LB) test for temporal independence up to lag K. The condensed diagnostic profiles are structured in Table 4.

Table 4: Summary of residual diagnostic tests for the GSTARX-IDW model

Diagnostic Test	Null Hypothesis (H_0)	Passed	Failed	% Violation
Kolmogorov-Smirnov (KS)	Residuals are normally distributed	0	45	100.00%
Ljung-Box (LB)	Residuals are independently distributed	38	7	15.56%

The asymptotic properties of the KS test reveal that 100% of the grid-specific residuals significantly deviate from a Gaussian distribution ($p < 0.05$), capturing heavy-tailed characteristics and high variance driven by the stochastic nature of weekly Fire Radiative Power (FRP) bursts. Meanwhile, the LB test demonstrates that the global space-time architecture successfully captures temporal dependencies in 38 grid cells, whereas a subset of 7 functional locations ($L_{14}, L_{20}, L_{29}, L_{34}, L_{41}, L_{44}, L_{46}$) exhibits persistent temporal autocorrelation ($p < 0.05$). This indicates that while the linear GSTARX framework captures the primary spatial-temporal structure, minor localized non-linear dynamics remain in specific locations.

These diagnostic outcomes highlight the intrinsic non-Gaussian and threshold behavior of localized wildfire intensities. Rather than modifying the point estimation procedure, these properties further motivate evaluating non-linear extensions (such as Threshold-GSTARX architectures) in future work. To transform the discrete grid point forecasts ($\hat{Y}_{t+h}$) generated by the estimated GSTARX model into a continuous hazard map for regional interpretation, Ordinary Kriging is subsequently applied directly to the point forecasts, as detailed in the geostatistical mapping phase.

3.4. Geostatistical Spatial Interpolation and Mapping

To formally verify the prerequisite of spatial dependence required for geostatistical spatial interpolation, Moran's I test for spatial autocorrelation was conducted across the grid centroids. The test revealed a strong and statistically significant positive spatial autocorrelation (Moran's $I = 0.4930$, $Z = 5.3292$, $p = 4.932 \times 10^{-8}$). This confirms that high FRP values exhibit significant geographic clustering across West Kalimantan, providing the robust statistical foundation necessary to implement Ordinary Kriging.

To establish the geostatistical structure for spatial continuous interpolation of the GSTARX point forecasts, empirical variograms were constructed and evaluated across four consecutive weekly lead times. The optimal theoretical spatial structure was determined by minimizing the Root Mean Square Error (RMSE) among Exponential, Spherical, and Gaussian candidates, as compiled in Table 5.

Spatial cross-validation was performed to assess the continuous interpolation accuracy of Ordinary Kriging via a leave-one-out cross-validation (LOOCV) framework. The resulting metrics demonstrated high predictive accuracy with minimal bias (RMSE = 0.2143, MAE = 0.1697, and Mean Error ME = −0.0064). Furthermore, spatial prediction uncertainty was quantified across the domain, yielding low prediction variances ($\sigma_k^2 \leq 0.05$) across areas with dense observation centroids. Uncertainty gradually increased toward unobserved boundary margins ($\sigma_k^2 \approx 0.20$), effectively capturing the spatial information decay inherent to geostatistical interpolation.

Table 5: Theoretical Variogram Model Selection and Parameters for Spatial Point Forecast Interpolation

Period	Candidate Model	Variogram RMSE	Selected Model	Nugget (C_0)	Partial Sill (C)	Range (a)
First Week	Exponential	**0.009635**	**Exponential**	0.000000	0.352184	2.010026
	Spherical	0.135643				
	Gaussian	0.013552				
Second Week	Exponential	0.008581	**Gaussian**	0.000000	0.133972	0.681973
	Spherical	0.103093				
	Gaussian	**0.004673**				
Third Week	Exponential	0.009241	**Gaussian**	0.008812	0.125990	0.751775
	Spherical	0.100635				
	Gaussian	**0.004027**				
Fourth Week	Exponential	**0.009451**	**Exponential**	0.000000	0.224023	1.610979
	Spherical	0.100316				
	Gaussian	0.010914				

For the first and fourth weeks, the spatial continuity of the point forecasts was best captured by the Exponential model, yielding the lowest RMSE values of 0.009635 and 0.009451, respectively. Conversely, the second and third weeks exhibited a smoother continuous behavior near the origin, making the Gaussian model the most suitable fit (RMSE of 0.004673 and 0.004027). These specific structural parameters (Nugget, Sill, and Range) were subsequently utilized as the mathematical foundation for continuous spatial surface mapping via Ordinary Kriging.

The spatio-temporal continuous surfaces of the predicted weekly Fire Radiative Power (FRP) for October 2025, obtained by applying Ordinary Kriging directly to the GSTARX-IDW point forecasts, are systematically visualized in Figure 4. The transition across the four successive weeks depicts a dynamic spatial pattern, capturing both the localized persistence of thermal anomalies and their gradual regional dissipation over time.

During the first week of October (Figure 4a), the study region exhibits elevated FRP levels, characterized by a prominent cluster (FRP values peaking near 6) localized in the southwestern and central-southern sectors of West Kalimantan. This spatial concentration aligns with the strong spatial lag dependence ($\mathbf{WY}_{t-1}$) identified in the model, where high fire intensity in a given grid cell is spatially associated with elevated thermal intensities in neighboring locations during the preceding week.

In the second week (Figure 4b), a contraction of the southern cluster is observed, although a core of high FRP values remains. Concurrently, a secondary localized thermal area appears in the northwestern coastal zone (around Mempawah and Sambas regencies), indicating spatial shifts in predicted fire activity.

By the third week (Figure 4c), the predicted spatial distribution shows localized activity in the west-central zone, whereas the eastern and northeastern highland sectors (e.g., Kapuas Hulu) consistently exhibit lower predicted risk levels (FRP ≤ 2) throughout the forecast window. This spatial variation is consistent with the localized exogenous diagnostics and spatial structure modeled across the grid network.

Finally, the fourth week of October (Figure 4d) shows a broader reduction in predicted FRP intensity across the region. The high-intensity clusters largely subside into lower thermal classes (FRP values between 2 and 4). This regional decline coincides with typical seasonal transitions in rainfall patterns across West Kalimantan, reflecting a weakening of weekly spatial-temporal persistence toward the end of the month.

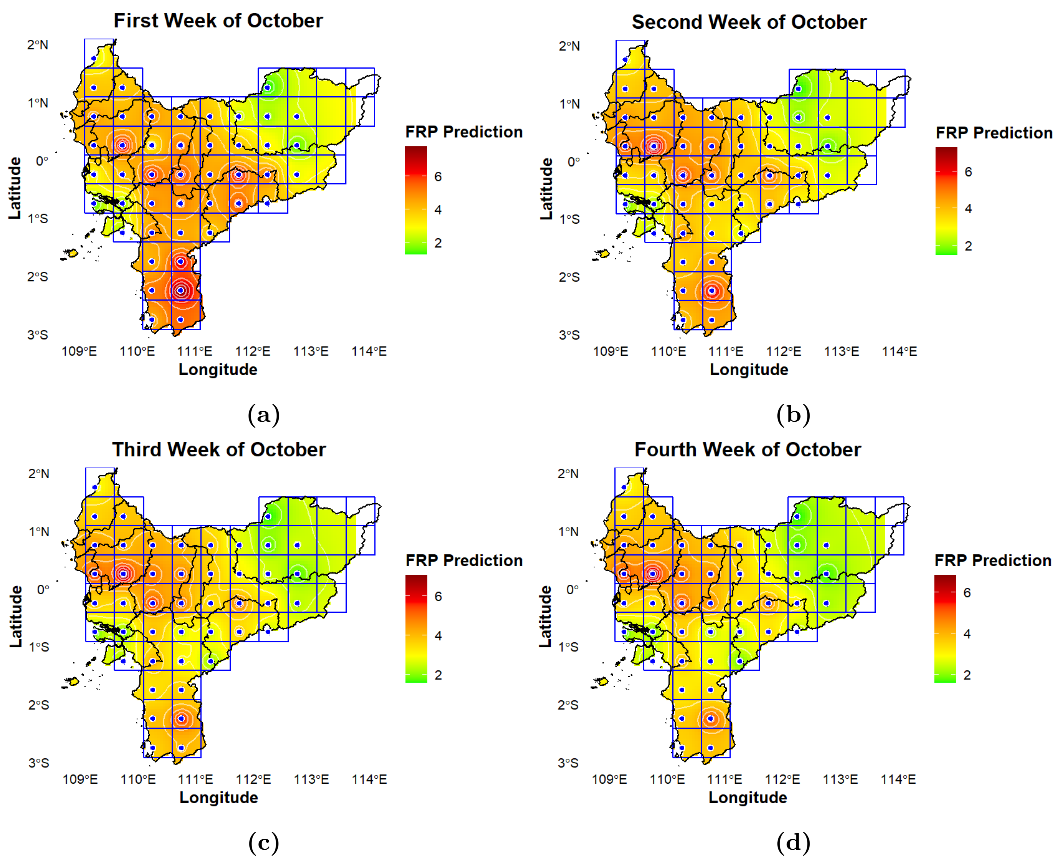

Fig. 4: Interpolated FRP forecast maps for October 2025 (a) first week, (b) second week, (c) third week, and (d) fourth week

To formally validate the predictive capabilities of the integrated spatio-temporal estimation and geostatistical mapping framework, a comprehensive error metric evaluation was conducted across out-of-sample lead times ($h = 1, 2, 3, 4$). The system's predictive power is assessed using Root Mean Squared Error (RMSE), Mean Absolute Error (MAE), and Mean Absolute Scaled Error (MASE). Table 6 outlines the compiled performance diagnostics comparing the proposed model against standard benchmark specifications.

Table 6: Out-of-sample predictive performance metrics across benchmark and spatio-temporal frameworks

Model Framework	**RMSE**	**MAE**	**MASE**
Naïve Forecasting Benchmark	1.4111	0.8729	1.0000
GSTAR-IDW (Univariate)	1.1743	0.8377	0.9597
GSTARX-Queen (Exogenous X_{t-1})	1.1489	0.8834	1.0120
GSTARX-IDW (Exogenous X_{t-1})	1.1322	0.8672	1.0006
GSTARX-IDW + Ordinary Kriging	1.1380	0.8736	1.0008

The out-of-sample predictive performance across the four-week forecast horizon confirms the global effectiveness of the spatial-temporal framework. Evaluating performance strictly at sampled grid centroids reveals that the discrete GSTARX-IDW model yields the highest overall point precision, achieving an RMSE of 1.1322, an MAE of 0.8672, and a MASE of 1.0006. From a benchmark perspective, a MASE value virtually equal to unity indicates that the linear spatio-temporal specification achieves predictive accuracy comparable to the standard naïve baseline (MASE = 1.0000). This metric highlights that while the linear spatio-temporal structure adequately captures the baseline dynamic trajectory of weekly FRP across West Kalimantan, localized high-frequency volatility and non-linear FRP bursts present ongoing structural forecasting challenges.

To bridge discrete point predictions with continuous regional risk interpretation, Ordinary Kriging is applied directly to these GSTARX-IDW point forecasts. Evaluating the resulting continuous hazard surface back at the sampled grid nodes yields an RMSE of 1.1380, an MAE of 0.8736, and a MASE of 1.0008. The marginal difference in error metrics (ΔRMSE = 0.0058) demonstrates that Ordinary Kriging effectively interpolates continuous risk fields across unobserved spatial domains without distorting point-forecast accuracy at sampled locations. Consequently, this integrated two-phase workflow provides a practical spatial-temporal baseline for short-term risk mapping in satellite-monitored tropical landscapes.

3.5. Limitations

Several methodological limitations of this study warrant consideration. First, the exclusion of zero-dominated grid cells ($L_{43} \ldots L_{52}$) to avoid matrix singularity introduces a potential localized selection bias, effectively restricting the temporal model's domain to active fire zones while relying on Ordinary Kriging for continuous spatial representation across unobserved regions. Second, the continuous linear formulation of the GSTARX model may exhibit reduced sensitivity during extreme, sudden fire-burst events that exceed linear threshold dynamics. Finally, the framework relies on satellite-derived observations from NASA's FIRMS, which are subject to cloud-cover obstruction and temporal satellite overpass gaps, necessitating continuous spatial refinement.

4. Conclusion

This study successfully developed and evaluated an integrated spatio-temporal forecasting framework combining the Generalized Space-Time Autoregressive with Exogenous Variables (GSTARX-IDW) model and Ordinary Kriging to predict weekly Fire Radiative Power (FRP) dynamics in West Kalimantan. The empirical findings reveal a near-absolute dominance of the spatial autoregressive component, which achieved statistical significance in 95.56% of the analyzed grid cells. This widespread significance strongly validates Tobler's First Law of Geography within regional wildfire distributions, proving that weekly fire intensity is heavily accelerated by the burning footprint of adjacent physical neighbors in the preceding week. Furthermore, while weekly land surface temperature exhibits high structural sparsity at a global level due to non-linear biophysical thresholds, the framework successfully isolated distinct localized relationships, exposing a clear geographic dichotomy that includes symmetric coupled behaviors, reversed polarity frameworks driven by deep peatland dry-out cycles, and isolated micro-environmental internal dependencies.

This research demonstrates the efficacy of a sequential hybrid GSTARX-IDW and Ordinary Kriging framework for spatio-temporal disaster risk assessment. By directly interpolating the k-step ahead point forecasts via Ordinary Kriging, the proposed approach successfully converts discrete centroid predictions into continuous spatial risk surfaces across unobserved regions. Evaluated through scale-independent metrics, the framework achieved a robust temporal fit with an RMSE of 1.1380, MAE of 0.8736, and a stable MASE of 1.0008, providing a competitive point forecast baseline alongside continuous spatial risk mapping capability. Despite its structural stability, this framework is limited by its continuous linear parameters, which lack the sensitivity to map sudden threshold triggers, and its reliance on secondary satellite observations from NASA's FIRMS that demand rigorous data-filtering protocols in zero-inflated, non-fire zones. Consequently, future research directives should pivot toward incorporating complex physical drought indices, such as the Keetch-Byram Drought Index (KBDI), and exploring non-linear threshold-GSTARX architectures to better capture the complex subsurface smoldering dynamics inherent to tropical peatland ecosystems.

CRediT Authorship Contribution Statement

Nurfitri Imro'ah: Conceptualization, Methodology, Writing–Original Draft. **Nur'ainul Miftahul Huda:** Data Curation, Formal Analysis, Writing–Review & Editing. **Yundari:** Software, Validation, Visualization. **Gita Fitriyana:** Software, Visualization.

Declaration of Generative AI and AI-assisted technologies

No generative AI or AI-assisted technologies were used during the preparation of this manuscript.

Declaration of Competing Interest

The authors declare no competing interests.

Funding and Acknowledgments

This research was supported and funded by the Faculty of Mathematics and Natural Sciences, Universitas Tanjungpura, through the DIPA Research Grant Scheme under Contract Nomor SP DIPA-139.03.2.693380/2026 Tanggal 01 Desember 2025.

Data and Code Availability

The FRP and Temperature datasets were obtained from the Fire Information for Resource Management System (FIRMS) and NASA MODIS, respectively, and are publicly available.

References

[1] Nur'ainul Miftahul Huda, Nurfitri Imro'ah, and Yousri Slaoui. "Analysis of Spatial Temporal Model with Intervention Effect on Forest Fires". In: *Journal of Statistical Theory and Practice* 20.1 (Nov. 2025). DOI: 10.1007/s42519-025-00517-4.

[2] Yundari Yundari, Nur'ainul Miftahul Huda, Udjianna Sekteria Pasaribu, Utriweni Mukhaiyar, and Kurnia Novita Sari. "Stationary process in GSTAR(1;1) through kernel function approach". In: *The 4th INDOMS International Conference on Mathematics and Its Application (IICMA 2019)*. Vol. 2268. AIP Publishing, 2020, p. 020010. DOI: 10.1063/5.0016808.

[3] Nur'ainul Miftahul Huda and Nurfitri Imro'ah. "New algorithm in detecting outliers from a spatial–temporal perspective in forest fire cases". In: *Spatial and Spatio-temporal Epidemiology* 57 (2026), p. 100804. DOI: 10.1016/j.sste.2026.100804.

[4] Utriweni Mukhaiyar, F T Nabilah, U S Pasaribu, and Nur'ainul Miftahul Huda. "The Space-Time Autoregressive Modelling with Time Correlated Errors for The Number of Vehicles in Purbaleunyi Toll Gates". In: *Journal of Physics: Conference Series* 2243.1 (2022), p. 012068. DOI: 10.1088/1742-6596/2243/1/012068.

[5] Utriweni Mukhaiyar, Nur'ainul Miftahul Huda, Kurnia Novita Sari, and Udjianna Sekteria Pasaribu. "Analysis of Generalized Space Time Autoregressive with Exogenous Variable (GSTARX) Model with Outlier Factor". In: *Journal of Physics: Conference Series* 1496.1 (Mar. 2020), p. 012004. DOI: 10.1088/1742-6596/1496/1/012004.

[6] Nur'ainul Miftahul Huda, Nurfitri Imro'ah, Hesty Pratiwi, and Muhammad Yahya Ayyash. "Minimal Grid Dimensions for High-Order Connectivity via 2-Distance Dominating Sets in Spatial-Temporal Analysis". In: *Applied Spatial Analysis and Policy* 19.2 (2026). DOI: 10.1007/s12061-026-09905-0.

[7] David Manley. "Scale, Aggregation, and the Modifiable Areal Unit Problem". In: *Handbook of Regional Science*. Springer Berlin Heidelberg, 2021, pp. 1711–1725. DOI: 10.1007/978-3-662-60723-7_69.

[8] Yohanes Setiawan, Regita Putri Permata, Adzanil Rachmadi Putra, Cisa Valentino Cahya Ramadhani, and Ryanta Meylinda Savira. "Generalized Space-Time Autoregressive with Exogenous Variable (GSTARX) and Transformer Architecture for Rainfall Forecasting". In: *Proceedings of the 2025 5th International Conference on Intelligent Cybernetics Technology & Applications (ICICyTA)*. IEEE, Dec. 2025, pp. 262–267. DOI: 10.1109/ICICyTA68677.2025.11362621.

[9] Zuleha Zuleha, Nur'ainul Miftahul Huda, and Nurfitri Imro'ah. "Comparing Areal and Grid Supports for Fire Radiative Power within a GSTAR $(p; \lambda_1, \lambda_2, \ldots, \lambda_p)$ Framework". In: *JTAM (Jurnal Teori dan Aplikasi Matematika)* 10.2 (Apr. 2026), pp. 378–395. DOI: 10.31764/jtam.v10i2.36663.

[10] Nurfitri Imro'ah, Nur'ainul Miftahul Huda, Hesty Pratiwi, and Muhammad Yahya Ayyash. "Spatio-temporal modeling of fire hotspots using GSTAR(1;1) model with meteorology based weight matrices". In: *Hacettepe Journal of Mathematics and Statistics* 54.6 (Dec. 2025), pp. 2525–2542. DOI: 10.15672/hujms.1726843.

[11] Hesty Pratiwi, Nurfitri Imro'ah, and Nur'ainul Miftahul Huda. "Forest Fire Analysis from Perspective of Spatial-Temporal Using GSTAR $(p; \lambda_1, \lambda_2, \ldots, \lambda_p)$ Model". In: *BAREKENG: Jurnal Ilmu Matematika dan Terapan* 19.2 (Apr. 2025), pp. 1379–1392. DOI: 10.30598/barekengvol19iss2pp1379-1392.

[12] Gita Fitriyana, Nurfitri Imro'ah, Nur'ainul Miftahul Huda, and Zuleha Zuleha. "Interpolation of Fire Radiative Power in West Kalimantan using Ordinary Kriging". In: *JTAM (Jurnal Teori dan Aplikasi Matematika)* 9.4 (Oct. 2025), p. 1287. DOI: 10.31764/jtam.v9i4.32643.

[13] Carolina Filizzola et al. "Fire Characterization by Using an Original RST-Based Approach for Fire Radiative Power (FRP) Computation". In: *Fire* 6.2 (Jan. 2023), p. 48. DOI: 10.3390/fire6020048.

[14] Elizabeth B. Wiggins et al. "High Temporal Resolution Satellite Observations of Fire Radiative Power Reveal Link Between Fire Behavior and Aerosol and Gas Emissions". In: *Geophysical Research Letters* 47.23 (Dec. 2020). DOI: 10.1029/2020gl090707.

[15] Zixun Dong, Change Zheng, Fengjun Zhao, Guangyu Wang, Ye Tian, and Hongchen Li. "A Deep Learning Framework: Predicting Fire Radiative Power From the Combination of Polar-Orbiting and Geostationary Satellite Data During Wildfire Spread". In: *IEEE Journal of Selected Topics in Applied Earth Observations and Remote Sensing* 17 (2024), pp. 10827–10841. DOI: 10.1109/jstars.2024.3403146.

[16] F Hikmawati, Suhartono, and D D Prastyo. "A Hybrid GSTARX-Jordan RNN Model for Forecasting Space-Time Data with Calendar Variation Effect". In: *Journal of Physics: Conference Series* 1752.1 (Feb. 2021), p. 012013. DOI: 10.1088/1742-6596/1752/1/012013.

[17] Sung Wook Kim, Felix Achana, and Stavros Petrou. "A bootstrapping approach for generating an inverse distance weight matrix when multiple observations have an identical location in large health surveys". In: *International Journal of Health Geographics* 18.1 (Nov. 2019). DOI: 10.1186/s12942-019-0189-5.

[18] Leonardo Ramos Emmendorfer and Graçaliz Pereira Dimuro. "A Novel Formulation for Inverse Distance Weighting from Weighted Linear Regression". In: *Computational Science – ICCS 2020*. Springer International Publishing, 2020, pp. 576–589. DOI: 10.1007/978-3-030-50417-5_43.

[19] Gita Fitriyana, Nurfitri Imro'ah, and Nur'ainul Miftahul Huda. "Interpolation of Fire Radiative Power Based on GSTAR Model Predictions with Queen Contiguity Weights Using Ordinary Kriging". In: *CAUCHY: Jurnal Matematika Murni dan Aplikasi* 11.1 (May 2026), pp. 16–31. DOI: 10.18860/cauchy.v11i1.37462.

[20] M.A. Oliver and R. Webster. "A tutorial guide to geostatistics: Computing and modelling variograms and kriging". In: *CATENA* 113 (Feb. 2014), pp. 56–69. DOI: 10.1016/j.catena.2013.09.006.

[21] Noel Cressie. *Statistics for spatial data*. John Wiley & Sons, 2015.

[22] Mohsin Khan, Mohammed M. A. Almazah, Asad EIlahi, Rizwan Niaz, A. Y. Al-Rezami, and Baber Zaman. "Spatial interpolation of water quality index based on Ordinary kriging and Universal kriging". In: *Geomatics, Natural Hazards and Risk* 14.1 (Mar. 2023). DOI: 10.1080/19475705.2023.2190853.

[23] Haiyang Xia, Song Zha, Jijun Huang, and Jibin Liu. "Radio environment map construction by adaptive ordinary Kriging algorithm based on affinity propagation clustering". In: *International Journal of Distributed Sensor Networks* 16.5 (May 2020), p. 155014772092248. DOI: 10.1177/1550147720922484.

[24] Andy H. Wong and Tae J. Kwon. "Development and Evaluation of Geostatistical Methods for Estimating Weather Related Collisions: A Large-Scale Case Study". In: *Transportation Research Record: Journal of the Transportation Research Board* 2675.11 (2021), pp. 828–840. DOI: 10.1177/03611981211020008.

[25] Timothy O. Hodson. "Root-mean-square error (RMSE) or mean absolute error (MAE): when to use them or not". In: *Geoscientific Model Development* 15.14 (2022), pp. 5481–5487. DOI: 10.5194/gmd-15-5481-2022.

[26] Philip Hans Franses. "A note on the Mean Absolute Scaled Error". In: *International Journal of Forecasting* 32.1 (Jan. 2016), pp. 20–22. DOI: 10.1016/j.ijforecast.2015.03.008.